ACS NANO

www.acsnano.org

Shaping the Color and Angular Appearance of Plasmonic Metasurfaces with Tailored Disorder

Florian Sterl, Ediz Herkert, Steffen Both, Thomas Weiss, and Harald Giessen*

Cite This: *ACS Nano* 2021, 15, 10318−10327

Read Online

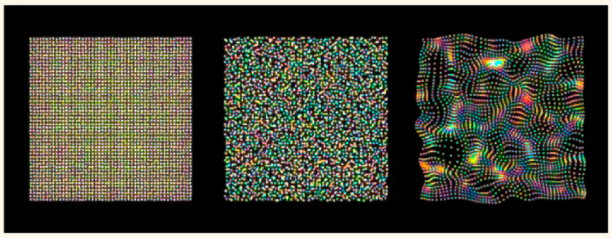

ABSTRACT: **The optical properties of plasmonic nanoparticle ensembles are determined not only by the particle shape and size but also by the nanoantenna arrangement. To investigate the influence of the spatial ordering on the far-field optical properties of nanoparticle ensembles, we introduce a disorder model that encompasses both "frozen-phonon" and correlated disorder. We present experimental as well as computational approaches to gain a better understanding of the impact of disorder. A designated Fourier microscopy setup allows us to record the real- and Fourier-space images of plasmonic metasurfaces as either RGB images or fully wavelength-resolved data sets. Furthermore, by treating the nanoparticles as dipoles, we calculate the electric field based on dipole−dipole interaction, extract the far-field response, and convert it to RGB images. Our results reveal how the different disorder parameters shape the optical far field and thus define the optical appearance of a disordered metasurface and show that the relatively simple dipole approximation is able to reproduce the far-field behavior accurately. These insights can be used for engineering metasurfaces with tailored disorder to produce a desired bidirectional reflectance distribution function.**

KEYWORDS: *plasmonics, metasurfaces, disorder, k-space imaging, microscopy, spectroscopy*

The concept of structural disorder in physical systems has attracted much attention in recent years, as it has been shown to define the optical properties of many different systems. Functional disorder occurs in nature, for example in flowers or beetle scales, determining the optical properties of these surfaces and improving, for example, temperature control and optical signaling.[1,2] This has fueled the development of bioinspired disordered materials.[3] Disorder-induced light scattering has brought forward random lasers,[4] disordered opaque media have been used as programmable optical circuits in combination with wavefront shaping,[5−7] and disorder-engineered metasurfaces have in turn been employed for wavefront shaping and high-resolution microscopy.[8] Disorder due to fabrication errors influences the optical properties of photonic crystals,[9] and nanostructures produced using electron-beam lithography typically suffer from structural disorder due to alignment errors and the proximity effect.[10,11] On the other hand, exploiting the effects of structural disorder has also brought forward applications such as photon trapping and localization of surface plasmon polaritons[12−14] and on-chip spectrometry.[15,16] Most notably, disordered arrangements of nanostructures have been used to determine the far-field optical properties of metasurfaces, with applications in structural colors[17−20] and enhanced light collection in thin-film solar cells.[21−24] Another application of tailored disorder in nanostructure arrangements is the suppression of grating modes to achieve an angle-independent response[25,26] or, in the opposite case, the realization of metasurfaces with a tailored, ultrahigh angular selectivity.[27]

The optical appearance of any surface can be characterized *via* its so-called *bidirectional reflectance distribution function* (BRDF). This quantity can be thought of as a measure of "shininess". A surface can act as a perfect mirror and thus reflect all incoming light into an angle equal to the angle of incidence. Such a reflection is called *specular*. On the other hand, incoming light might be isotropically scattered into all directions, so that the angle of incidence cannot be determined from the distribution of reflected light anymore. This is called *diffuse* reflection or scattering. Light absorption and/or transmission by the surface can furthermore decrease the

Received: March 24, 2021
Accepted: June 4, 2021
Published: June 11, 2021

https://doi.org/10.1021/acsnano.1c02538
ACS Nano 2021, 15, 10318−10327

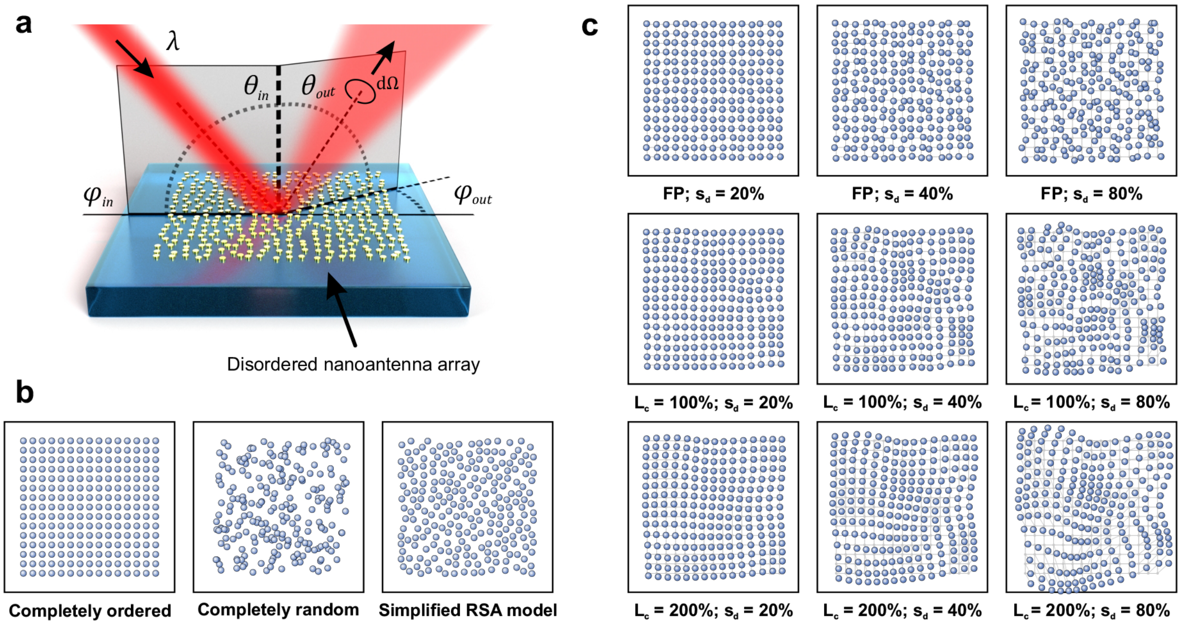

Figure 1. (a) Schematic of the parameters involved in the definition of the bidirectional reflectance distribution function (BRDF). We investigate the influence of spatial disorder in plasmonic nanoparticle ensembles on the far-field appearance, using different disorder models. In addition to completely randomized and hyperuniform disorder (b), we employ short-range "frozen-phonon" (FP) disorder with varying disorder strength s_d as well as correlated disorder with varying correlation length L_c (c).

total amount of reflected light. Additionally, these effects can vary with wavelength. The BRDF contains a complete description of the angle- and wavelength-dependent far-field reflectance of a surface:[28]

$$\mathrm{BRDF}(\theta_{\mathrm{in}}, \varphi_{\mathrm{in}}, \theta_{\mathrm{out}}, \varphi_{\mathrm{out}}, \lambda) = \frac{\mathrm{d}L_{\mathrm{out}}(\theta_{\mathrm{out}}, \varphi_{\mathrm{out}}, \lambda)}{\mathrm{d}E(\theta_{\mathrm{in}}, \varphi_{\mathrm{in}}, \lambda)} \tag{1}$$

Here, θ_{in} and φ_{in} are the polar and azimuthal angles of incidence, while θ_{out} and φ_{out} are the angles of reflection/scattering, as illustrated in Figure 1a. In daily life, most surfaces can be considered rotationally symmetric, so that φ_{in} can be ignored. L_{out} is the spectral radiance leaving the surface (expressed in units of power per unit area per unit solid viewing angle dΩ), while E is the spectral irradiance of the sample (units of power per unit area). In a more generalized definition, the polarization of incoming and reflected light can be added as a variable as well.

The BRDF is widely used in, for example, computer graphics, to accurately reproduce the appearance of real-world surfaces and materials in photorealistic rendering, along with inverse problems such as object recognition.[29] Another application is the characterization of surface albedo and vegetation patterns *via* satellite imaging. BRDF measurements at these size scales are typically done by goniometer-based setups, in which a light source and a detector are moved through a set of angles relative to a surface.[30] At the sub-100 μm size scale of the work presented here, it is in principle possible to record BRDF measurements using goniometric ellipsometry setups (actually designed to determine the dielectric function of a material), but these typically suffer from a limited spatial resolution.

An established technique for characterizing the angle-dependent optical far-field behavior of a microscale sample is so-called *Fourier microscopy*, also called *k-space microscopy* or *back focal plane microscopy*.[31,32] The concept of Fourier microscopy has, for example, been employed to investigate the far-field behavior of single plasmonic nanostructures[33,34] and to characterize nanostructures with tailored directional emission behavior.[35−39] The combination of Fourier microscopy with imaging spectroscopy has furthermore proven useful for microellipsometry[40,41] and to fully characterize the angle- and wavelength-dependent behavior of complex plasmonic systems, such as plasmonic lenses,[42] plasmonic perfect absorbers,[25] and plasmonic sensor structures.[26]

In Fourier microscopy, one observes not the front focal plane (which is the image plane) of the microscope objective but the back focal plane (BFP). The radial coordinate **k** in the BFP corresponds to the angle in the image plane *via*

$$\mathbf{k} = \begin{bmatrix} k_x \\ k_y \end{bmatrix} = n \begin{bmatrix} \sin\theta\,\cos\varphi \\ \sin\theta\,\sin\varphi \end{bmatrix} \tag{2}$$

with n the refractive index between the objective front lens and the image plane. The BFP image thus contains information about all accessible angles θ_{out} and φ_{out}, limited by the objective NA. By carefully manipulating the sample illumination, the incident angles (or range of angles) θ_{in} and φ_{in} can be varied as well, so that it is possible to reconstruct the full BRDF from k-space measurements.

When speaking about disorder, the main question is how one *defines* disorder and, moreover, how one *quantifies* it. In positional disorder, that is, disorder in the distribution of particles across a surface, one could define the two extreme cases of "completely ordered" and "completely randomized", as illustrated in Figure 1b. In the completely ordered case, each particle occupies a position out of a predefined discrete set, such as a rectangular or hexagonal lattice. In the completely randomized case, any position is accessible and each particle is positioned at random (x, y) coordinates, without being influenced by the other particles at all. This fully randomized distribution inevitably leads to cluster formation. For objects of finite size, it leads to overlapping as well and is thus not necessarily a realistic model for nanoparticle distribution.

In a more realistic scenario, nanoparticles are randomly distributed while maintaining a certain minimum distance to each other due to repulsive forces. This is, for example, the case in many colloidal fabrication methods.[43−46] Such quasi-randomized distributions can be generated by random sequential adsorption (RSA)-based models.[47] Figure 1b shows an example of the simplified RSA model, in which the minimum interparticle spacing was set to preserve the number of particles per unit area with respect to the completely ordered case. Other models for generating quasi-randomized (or, by an equally valid term, quasi-periodic) distributions are Matérn-type distributions[18] and the so-called Penrose tiling, which has also been observed in quasi-crystalline materials.[48,49] An extensive overview of disorder models and methods of characterization can, for example, be found in the work of Torquato and Stillinger.[50]

However, in this work, we aim for a *quantification* of the influence of structural disorder on the optical properties of plasmonic metasurfaces. This requires a disorder model that allows for a tunable *degree* of disorder in reproducible disordered arrays. We make use of the model employed in nanowire-based photonic crystals by Nau *et al.*[51,52] In this model, which is comparable to the method used by Zhang *et al.*,[53] particles are randomly displaced from their initial lattice positions, with a maximum displacement defined as the *disorder strength*. This configuration is also called "frozen-phonon"-type disorder or uncorrelated disorder, since the elements do not influence each other. Thus, only short-range disorder is introduced, while long-range order is preserved. A disorder strength of zero corresponds to the original lattice. In addition to the displacement, a *correlation* can be introduced.

In the case of frozen-phonon disorder in a perturbed lattice consisting of $n_x \times n_y$ elements, the coordinates of element $i = 1, ..., N$ with $N = n_x n_y$ are given by

$$\begin{bmatrix} x \\ y \end{bmatrix}_i = \begin{bmatrix} x_0 \\ y_0 \end{bmatrix}_i + \begin{bmatrix} \Delta x \\ \Delta y \end{bmatrix}_i \tag{3}$$

with x_0 and y_0 the initial lattice coordinates corresponding to element i, and Δx and Δy the displacement of the element from its lattice position. Several different distributions can be used for the randomly chosen values of Δx and Δy. In the work of Nau *et al.*, a Gaussian distribution was used, in which case the full width at half-maximum (fwhm) of the distribution is a measure for the disorder strength. In this work, we consider a rectangular distribution, in which the disorder strength s_d is defined as the maximum displacement that any element can have from its lattice position in both directions:

$$|\Delta x|, |\Delta y| \leq s_d P \tag{4}$$

with P the lattice constant of the initial lattice. This definition is chosen to make s_d a dimensionless factor, normalized to the lattice constant.

This distribution is used to prevent the occurrence of outliers far outside the disordered array. The frozen-phonon disorder can thus be thought of as placing each particle at a random position within a square centered at the lattice position, with s_d defining the size of this square. In the case of a nonisotropic periodicity and/or a nonisotropic disorder strength, the square is replaced by a rectangle.

The disorder model can be extended to include *correlated disorder*, also called long-range disorder. In this case, each shifted element adds an additional shift to all other elements, which is proportional to its own shift *via* a correlation function $C(r)$, with r the distance between the two points. For each element i, a random shift $[\Delta x, \Delta y]^T$ is generated as before. Then, all elements $j \neq i$ are assigned an additional shift $[\Delta x, \Delta y]_i^T C(r_{ij})$. After this is done for all N positions, the coordinates of element i are given by

$$\begin{bmatrix} x \\ y \end{bmatrix}_i = \begin{bmatrix} x_0 \\ y_0 \end{bmatrix}_i + \begin{bmatrix} \Delta x \\ \Delta y \end{bmatrix}_i + \sum_{j \neq i} \begin{bmatrix} \Delta x \\ \Delta y \end{bmatrix}_j C(r_{ij}) \tag{5}$$

In our implementation, we use a correlation function with a Gaussian shape:

$$C(r_{ij}) = \exp\left[-\left(\frac{r_{ij}}{2L_c P}\right)^2\right] \tag{6}$$

so that the correlation length L_c (again normalized to P) is directly related to the fwhm of the Gaussian curve ($\text{fwhm} = 2\sqrt{2\ln 2}\, L_c P$). Figure 1c displays several examples of disordered arrangements generated by the model described above, for different values of both s_d and L_c.

The algorithm for generating sets of disordered positions thus uses the number of positions n_x, n_y, the disorder strength s_d, the correlation length L_c, and the periodicity of the original lattice P as input parameters. To make the disorder model size-independent, L_c and s_d are expressed in terms of P. In our implementation, the shift values Δx, Δy are generated using the MatLab internal pseudorandom number generator (RNG), which uses a seed value as input to initiate the set of pseudorandom numbers. Each combination of s_d and L_c can thus produce an infinite number of different realizations, as every RNG seed value results in a unique set of positions. Increasing either disorder parameter while keeping the seed value fixed results in all particles being shifted further in the same direction, as one can recognize in the examples in Figure 1c.

RESULTS AND DISCUSSION

The introduction of structural disorder into arrays of nanoparticles suppresses the angle-dependent far-field features that arise from the ordering itself, such as the Rayleigh anomalies[54] and quasi-guided modes.[55] These features manifest themselves in the angle-dependent transmittance and/or reflectance.

Figure 2 displays a set of angle-resolved transmittance spectra for different disordered Au nanodisk arrays (diameter d = 120 nm, height h = 60 nm, P = 500 nm), recorded using a microspectroscopy setup extended with a modified 4-f setup[56] (see the Supporting Information for a detailed description). The nanoparticle arrays are embedded in a layer of IC1-200 spin-on dielectric, which closely matches the refractive index of the SiO_2 substrate. Panel (a) shows the reflectance of an unperturbed array, for s and p polarization. The observed features can be attributed to the lattice's Rayleigh anomaly and to waveguide modes in the IC1-200 layer.[26] If uncorrelated disorder is introduced [panel (b)], these features gradually become less sharp with increasing s_d. At a disorder strength of 100%, no periodicity-induced modes are distinguishable

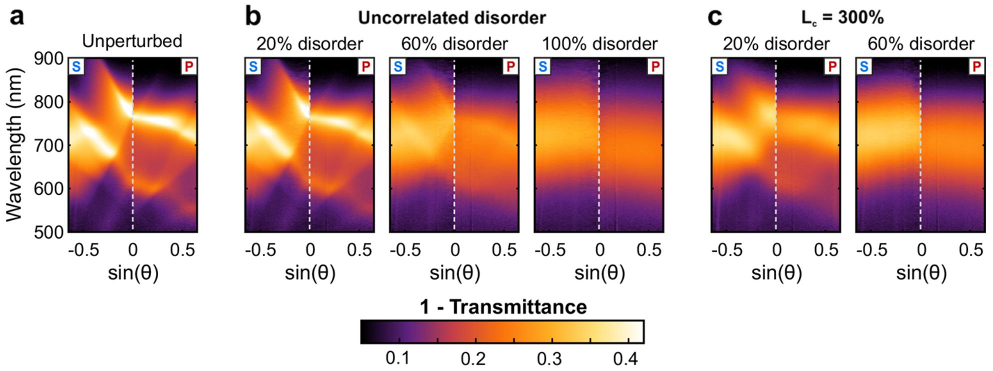

Figure 2. Measured *k*-space transmittance spectra of disordered Au nanodisk arrays (d = 120 nm, h = 60 nm, P = 500 nm), for (a) the unperturbed array, (b) arrays with frozen-phonon disorder with increasing disorder strength s_d, and (c) arrays with correlated disorder (L_c = 300%). Each set of positions is generated using the same random number generator seed value.

anymore. If a nonzero correlation length is added to the disorder [panel (c)], the features disappear at a smaller s_d value. At L_c = 300%, the *k*-space spectrum for s_d = 60% cannot be distinguished from the spectrum for s_d = 100% in the uncorrelated case. This indicates that the lattice-induced spectral features in bright-field spectral measurements are primarily determined by the *long-range* order of the sample, which diminishes much faster with s_d if L_c is increased. Since short-range order appears to be of no significant influence on the bright-field transmittance spectra, different combinations of L_c and s_d can produce the same result. These measurements can thus not be used to *identify* the disorder in the sample.

The far-field optical behavior of a periodic structure is dominated by diffraction effects. To characterize the influence of disorder on the optical response, it is thus necessary to image the diffraction. In the previous bright-field transmittance measurements, the diffraction orders are not directly visible. The signal measured at a certain angle (θ, φ) consists of the bright zeroth-order transmittance of light incident at the same angle, overlapped with diffracted light from all other incident angles. To image the diffraction orders, the range of incident angles must be reduced to a minimum. This can be achieved by illuminating the sample with a collimated beam, in other words with near-zero NA. By replacing the spectrometer with a CCD camera and by using a high-NA oil immersion objective, we record real-space and *k*-space RGB images with a maximum collection angle of approximately 69°. In the intermediate Fourier plane, an opaque stop can be inserted to block the zeroth-order reflection, which is far brighter than the diffracted/scattered light (see the Supporting Information). For these measurements, we use nanodisks made of aluminum rather than gold, as the plasmonic resonance of Al disks lies at shorter wavelengths and the structures thus show a clear response throughout the entire visible range.

Figure 3 displays a set of real-space and *k*-space RGB images of disordered Al nanoparticle ensembles, generated *via* completely randomized positions, *via* the simplified RSA model, and using frozen-phonon (uncorrelated) and correlated disorder. Each array is generated using the same seed value. The base lattice periodicity is 500 nm, which is above the diffraction limit of the microscope objective, so that the individual structures can be distinguished. In the completely randomized ensemble, overlapping structures exist (see the SEM images provided in the Supporting Information). These lead to very strong local scattering peaks, as the overlapping nanoparticles effectively form nanoantennas with a much higher scattering cross-section than the individual Al disks. In the simplified RSA model, the intensity distribution is again much more uniform, while the color impression is much more diverse than in the unperturbed case.

If frozen-phonon disorder is introduced, a somewhat different picture arises. The overall color impression remains comparable to the base lattice. As s_d increases, more particles appear at very small distances from each other, again leading to stronger intensity peaks in the real-space image. Correlated disorder leads to another clearly recognizable effect. Different colors occur again, but in this case, areas or “patches” of locally similar colors can be recognized. These areas occur at sizes in the order of the correlation length L_c, as the correlation leads to the formation of locally similar interparticle distances. This indicates that one can think of a lattice perturbed by correlated disorder as a set of different smaller lattices, each with its own periodicity in x and y direction and with its own orientation. As s_d increases, very bright patches occur again. Similar to the uncorrelated case, these can be attributed to particles that are very close together. In this case, the correlation length causes the formation of patches of closely spaced particles, leading to larger areas of high intensity. At the same time, large areas of very large interparticle spacing are formed as well, leading to the formation of “dark” areas alongside the “bright” ones. It should be noted that the colors in the very bright patches are not always reproduced accurately, since the high intensity can lead to oversaturation of the CCD camera pixels (while reducing the exposure time would have significantly increased the noise in the darker areas).

In the *k*-space images (Figure 3b), the different disorder types can clearly be distinguished from one another as well. In the unperturbed grid, the first-order diffraction leads to sharp peaks at scattering angles determined by the lattice period and the wavelength ($\sin\theta = \lambda/nP$). In the case of fully randomized positions, no sharp features can be seen anymore, but rather scattering in all directions occurs. This can also be interpreted as an overlap of diffraction orders arising from many different lattices with random orientations and periodicities. In the case of simplified RSA disorder, the rotational symmetry of the diffraction pattern is maintained, but the angle-dependence is not. Light is diffracted into large angles, similar to the diffraction of the unperturbed lattice. The diffraction pattern of this disordered array can thus also be interpreted as overlapping diffraction patterns from many arrays with different orientations, but with *similar* periodicities. The range of angles into which the light is diffracted is in this

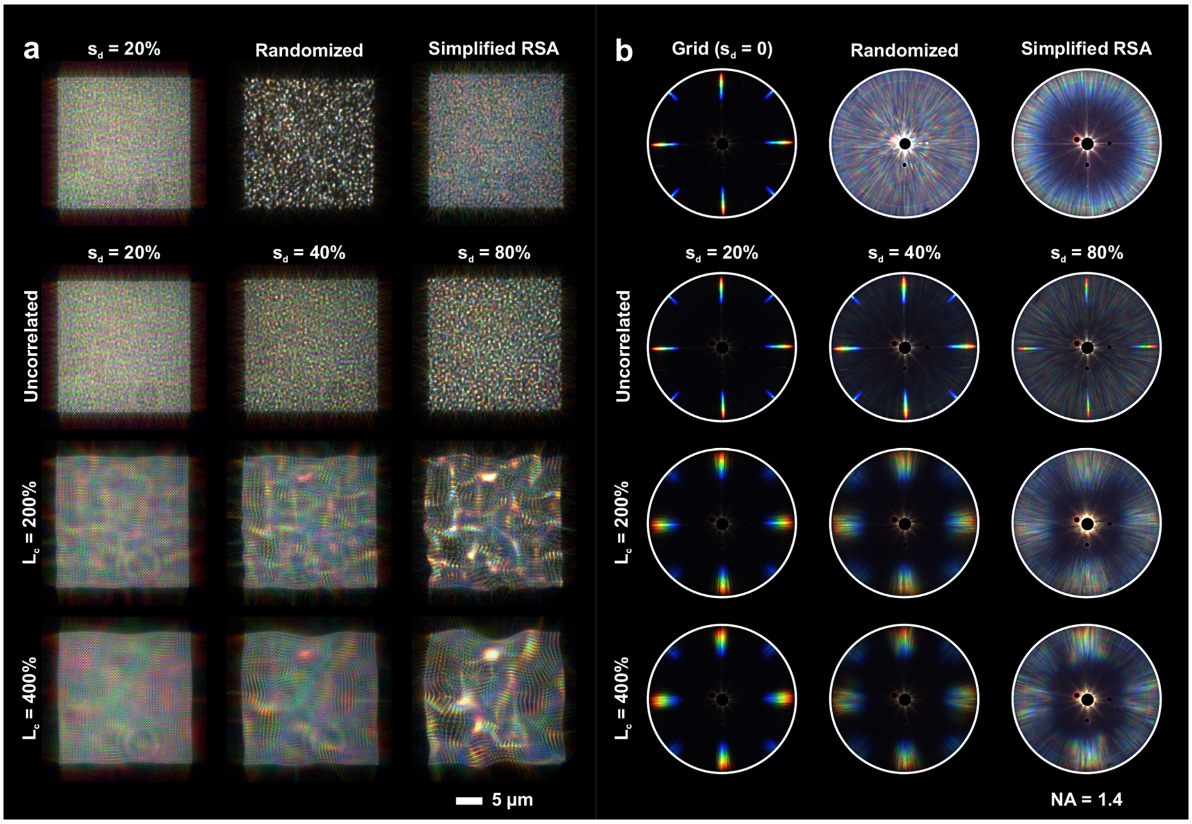

Figure 3. Real-space (a) and *k*-space (b) RGB reflected images of different disordered arrays of 50 × 50 Al nanodisks (d = 120 nm, h = 60 nm, P = 500 nm) at normal incidence. Each set of positions is generated using the same random number generator seed value.

case determined by the minimum distance s_{min} used for generating the set of positions.

In the case of uncorrelated disorder, isotropic scattering can be recognized as well. As s_{d} increases, the first-order diffraction peaks decrease in intensity, while a roughly isotropic background signal occurs, which increases in intensity. The introduction of a correlation length has a clearly different effect. In this case, the diffraction orders do not disappear, but show a *broadening* in the polar as well as the azimuthal angle. This confirms the intuitive picture of an array with correlated disorder as a superposition of gratings with different orientations and periodicities. Furthermore, high values of L_{c} and s_{d} at the same time lead to a strong enhancement of this broadening, as the variation in "local" periodicity and angle is increased. Nevertheless, diffraction/scattering into small angles still does not appear.

The *k*-space images in Figure 3b indicate that short-range and long-range order have distinct effects on the diffraction behavior. If only short-range disorder is introduced, but long-range order is still given (in the case of uncorrelated disorder), the diffraction orders of the base lattice can still be recognized. As the disorder strength increases, an isotropic scattering background occurs. The relative intensities of both features depend on the disorder strength. In contrast, if long-range disorder is introduced, while some short-range order is maintained (in the case of correlated disorder), a *broadening* rather than a *weakening* of the first-order diffraction is observed. This also means that the diffraction patterns in these "dark-field" *k*-space images can be used to *identify* the type of disorder present in the array, in contrast to bright-field measurements.

However, the observations described above are only valid if the first- or higher-order diffraction from the base lattice is collected by the microscope objective, in other words, for periodicities above the diffraction limit. If P is decreased, this is not the case anymore. Figure 4 shows real-space RGB images of Al nanodisk arrays using a subset of the disorder parameters used in Figure 3, but with a base lattice period of 250 nm instead of 500 nm. This means that the average interparticle spacing is *below* the diffraction limit, so that the individual particles cannot be resolved anymore. The overall effects are nevertheless similar. A larger s_{d} value leads to more variation in color, while the introduction of correlation leads to the formation of dark and bright patches at typical sizes scaling with L_{c}.

The loss of spatial resolution in Figure 4a with respect to Figure 3a is directly connected to the loss of first-order diffraction in the collected *k*-space image. Nevertheless, the *k*-space images recorded on these subdiffraction disordered arrays hold some interesting information as well. As shown in Figure 4b, a broadening of the zeroth-order diffraction (reflection) can be recognized in the case of correlated disorder. For lattices with only very little disorder, only a cross-shaped diffraction pattern is observed. This can be understood as diffraction caused by the square-shaped array as a whole, which acts as a single diffracting object. As L_{c} and s_{d} are increased, this shape is blurred. Together with the formation of "bright" and "dark" patches, this leads to broadening of the specular reflection.

To verify the accuracy of the recorded RGB images and to characterize the influence of the introduced disorder on the spectral distribution of the reflectance, we additionally perform

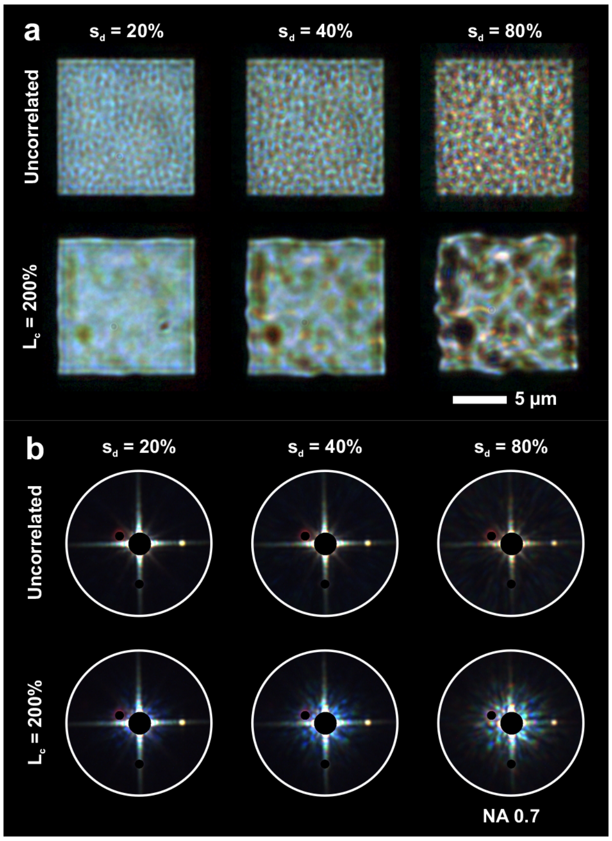

Figure 4. Real-space (a) and *k*-space (b) RGB reflected images of six different disordered arrays of 50 × 50 Al nanodisks (d = 120 nm, h = 60 nm, P = 250 nm) at normal incidence. Each set of positions is generated using the same random number generator seed value.

hyperspectral reflectance measurements using the motorized sample stage of the microscope. Corresponding results can be found in the Supporting Information.

In addition to the optical measurements, we implemented a calculation model to predict the far-field appearance of a disordered ensemble of plasmonic nanoparticles. In principle, it would be possible to calculate the optical far field of such an ensemble using finite-element or FDTD methods, but due to the large number of particles involved, this is an unpractical approach. Instead, we approximate each particle as a point dipole and calculate the interparticle interaction. Despite being a relatively simple model, the discrete dipole approach (DDA) has already been proven to mimic the behavior of even relatively complex plasmonic systems with a high degree of accuracy.[57]

In the dipole approximation, each particle is characterized by its polarizability α. In small spherical particles, α is isotropic, but for more complex particle shapes, this is not the case anymore. The polarizability can thus not be written as a scalar, but must be expressed as a *tensor*. The expression for the particle's dipole moment then reads

$$\mathbf{p} = \varepsilon_0 \varepsilon_e \hat{\alpha} \mathbf{E}_0 \tag{7}$$

with ε_e the dielectric function of the environment and $\hat{\alpha}$ the polarizability tensor. $\mathbf{E}_0$ represents the background electric field at the center of the particle. In the case of a disk-shaped particle of arbitrary size, no direct analytic expression for $\hat{\alpha}$ exists. Nevertheless, $\hat{\alpha}$ can be "reverse-engineered" if the electric field is known[57] (see the Supporting Information for further details).

The next step is to introduce coupling between particles in an ensemble of arbitrary size. If each dipole i at a location $\mathbf{r}_i$ is assumed to interact with all other dipoles $j \neq i$, the local electric field at $\mathbf{r}_i$ is equal to the sum of the incident electric field $\mathbf{E}_0$ and the electric field radiated by all other dipoles:

$$\mathbf{E}_i(\mathbf{r}_i) = \mathbf{E}_0(\mathbf{r}_i) + \sum_{j \neq i} \mathbf{E}_j(\mathbf{r}_i) \tag{8}$$

in which the fields at $\mathbf{r}_i$ and $\mathbf{r}_j$ are related *via* the free space Green tensor.[14] *Via* eq 7, this leads to a large set of coupled equations, which must be solved to obtain the electric field at each position in the ensemble of dipoles. By applying the near-to-far field conversion proposed by Yang *et al.*,[58] in which an incoming test plane wave $\mathbf{E}_0$ is projected on the scatterers in order to derive the electric field in a surrounding surface (in our case a plane at a typical distance of 1 nm above the dipole ensemble), the *k*-vector-resolved intensity radiated by the full dipole ensemble can be calculated. The result, truncated at $\sqrt{{k_x}^2 + {k_y}^2}/k \leq 1$, gives the total intensity radiated into the far field. This corresponds to the Fourier image that would be visible in a Fourier microscopy setup. To simulate the effect of a microscope objective with a limited NA, the truncation can also be performed at $\sqrt{{k_x}^2 + {k_y}^2}/k \leq \mathrm{NA}/n$. Furthermore, applying an inverse Fourier transform to the obtained *k*-vector-resolved intensity gives the corresponding real-space intensity distribution. This transform is analogous to the effect of adding a lens behind the Fourier plane to retrieve the real-space image (see Figure S2 of the Supporting Information).

By repeating this procedure for different wavelengths, the spectrally resolved reflected *k*-space and real-space images of a predefined ensemble of plasmonic nanoantennas, illuminated from a certain angle, can thus be extracted. By varying the angle of incidence of the incoming electric field $\mathbf{E}_0$ as well, it is in principle possible to obtain a full data set in which the reflected intensity as a function of wavelength and observation angle is related to the angle of incidence. This data set would, in other words, provide the full BRDF of the nanoparticle ensemble and thus contain all the necessary information for a full characterization of the far-field behavior of the metasurface. To visualize the response in the visible wavelength range, the three-dimensional data cube of reflectance *vs* position or *k*-vector can also be converted to color images, which can easily be compared to optical measurements. A detailed explanation of the conversion from spectral data to visible colors can be found in the Supporting Information.

It is also possible to include particles of different sizes, shapes, orientations, or even materials in the calculation. As long as the polarizability tensor $\hat{\alpha}$ is known for each particle, the electric field can be calculated *via* the coupled equations given by eq 8. By establishing a database of $\hat{\alpha}$ for many different particles, the dipole coupling model thus becomes a widely applicable tool for predicting the far-field behavior of disordered plasmonic metasurfaces.

To validate our calculation method, we compare calculated spectral responses of single nanodisks of different materials and diameters to single-particle dark-field microspectroscopic measurements. For Au nanodisks, this comparison reveals an almost perfect match. For Al particles, a red-shifted plasmonic

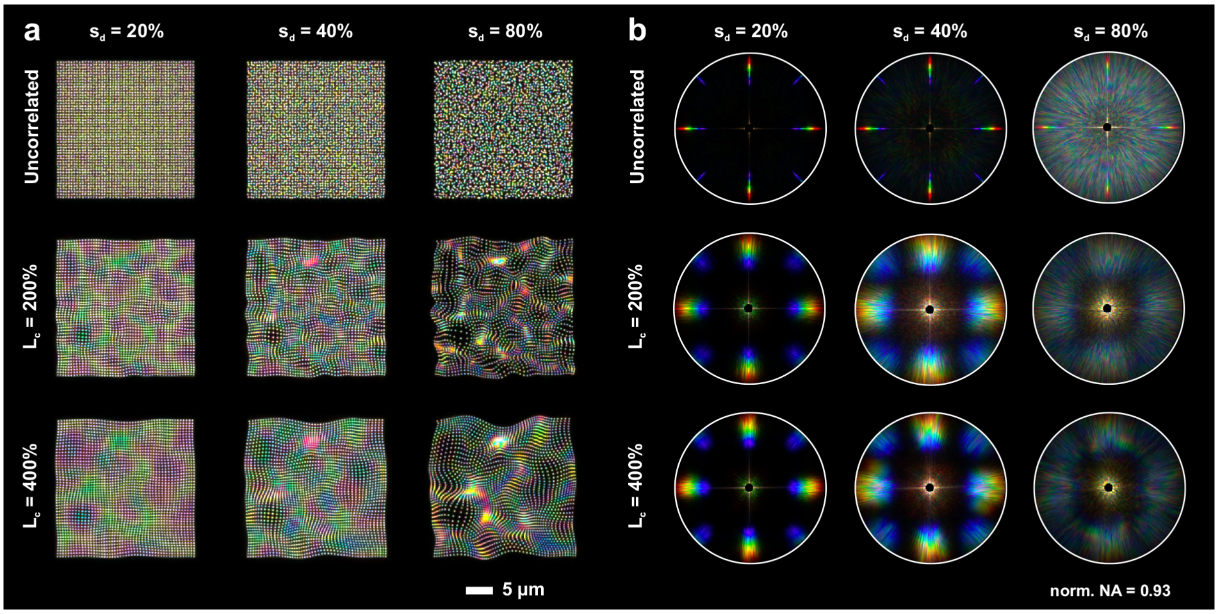

Figure 5. Calculated real-space (a) and *k*-space (b) RGB images of nine different disordered arrays of 50 × 50 aluminum nanodisks (d = 120 nm, h = 60 nm, P = 500 nm) at normal incidence, using the same sets of positions as in the measurements shown in Figure 3.

resonance is observed compared to the calculations, which can be explained by oxidation of the Al particles.[59] An example of the results can be found in the Supporting Information (Section 8). Furthermore, we compare the calculated spectral responses produced by the dipole model to calculations using finite-element calculation software (Comsol Multiphysics). Specifically, we perform calculations on a system of two Au nanodisks with a decreasing interparticle distance. The results, which can be found in Section 9 of the Supporting Information, show a very good agreement at interparticle distances down to 20 nm. Only at even smaller distances does additional electric field enhancement occur in the small gap between the particles, which leads to a higher scattering cross-section. As the dipole model does not consider the finite size of the individual particles, the agreement is thus not perfect anymore at very small particle separations. However, this plays only a limited role in large ensembles of particles, such as our disordered metasurfaces.

Figure 5a displays calculated real-space and *k*-space RGB images of disordered Al nanoparticle arrays, using the same disorder parameters as the recorded images shown in Figure 3. A comparison between the calculated and measured images reveals an astonishing agreement. Not only are the typical features of diffraction broadening and isotropic background scattering reproduced with a very high accuracy, but also the general color impression is very similar. Individual patches of color in the real-space images can be one-to-one identified in the measurements. The remaining difference can be attributed to the Al oxidation in combination with the different methods through which the color is generated. In the calculations, the conversion from spectral intensity to color is performed *via* a color model designed to mimic the human eye. In the measurements, the color follows from the spectral sensitivity of the CCD camera (see the Supporting Information). Furthermore, the nonuniform light source spectrum has an influence as well. In the measurements, this influence is compensated by white calibration of the camera, but cannot be fully omitted nonetheless.

The very good agreement between our measurements and numerical calculations demonstrates that the dipole approximation is able to predict the behavior of even relatively complex nanoparticle arrangements to a very high degree. The agreement is striking, especially since higher-order multipoles and, thus, their impact on the near-field coupling between particles at very short separation distances are not considered in the dipole model. Neither do the calculations take overlapping particles that effectively form one larger nanoantenna into account. Our results thus show that, while such effects may influence the electric field locally, they do not appear to be decisive for the overall far-field behavior of the ensemble. This demonstrates that our dipole-interaction-based calculation model is a very useful tool for predicting the optical far-field behavior of disordered plasmonic arrays. It can be used not only to verify optical measurements but also to calculate the fully wavelength-resolved BRDF of nanoparticle ensembles. This can, in turn, be used to determine the necessary combination of disorder parameters to realize a certain desired optical appearance. The relatively simple dipole model is thus ideal for the *engineering* of tailored disorder in plasmonic metasurfaces.

CONCLUSIONS

We have investigated the influence of structural disorder on the optical far-field response of plasmonic nanoantenna arrays. We have introduced a disorder model that uses two disorder parameters, namely, the disorder strength and the correlation length. To quantify the influence of both parameters, we have performed bright-field *k*-space microspectroscopic measurements as well as real-space- and *k*-space-resolved imaging measurements with near-normal incidence and high collection NA. The measurement results reveal that an increase of both disorder parameters inevitably leads to a broadening of the lattice-based features in the bright-field measurements, which can be attributed to a loss of long-range order despite the preservation of short-range order. However, a conclusion about the short-range order cannot be drawn exclusively from these bright-field measurements. In the measurements recorded at near-zero incidence, in contrast, both disorder parameters reveal a clearly distinguishable influence, manifesting in a weakening of the diffraction orders and the emergence of isotropic scattering as well as a significant broadening of the diffraction orders. This means that the surface appearance is gradually shifted from specular to diffuse in a controlled manner.

We have furthermore verified these observations using a calculation approach based on dipole−dipole interaction, which shows very good agreement with the measurement results. This relatively simple calculation approach can thus be widely applied in future investigations of disordered nanoplasmonic systems with other types of disorder, such as size disorder[20] or orientational disorder,[60] or combinations of different disorder types.[53] Another highly interesting prospect for the application of disordered plasmonic systems is the use of tailored disorder to engineer a desired far-field response *via* inverse design algorithms,[27] for which the comparably short calculation times due to the applied approximations are of great advantage. This holds potential use in the design and fabrication of nanoparticle coatings to generate desired appearances of surfaces, but also for the design of beam-steering devices and flat metalenses.[61,62] The dipole model thus also provides a highly useful tool for the design of such nanoplasmonic devices.

METHODS

Fabrication. For the sample fabrication, a cleaned SiO_2 substrate is spin-coated with resist (PMMA) for patterning in an electron-beam lithography system (RAITH eLINE Plus). After resist development, metal is deposited on the substrate with a Pfeiffer Vacuum PLS 500 electron-beam-assisted evaporation system, followed by resist lift-off in NEP. The structures are embedded in an approximately 200 nm thick layer of spin-on dielectric coating (IC1-200, Futurrex, Inc.), which serves a dual purpose: It protects the particles, and it nearly matches the refractive index of the glass substrate (nIC1-200 = 1.41), thus suppressing the influence of the interface. This is especially important for the comparison to numerical simulations (see the Supporting Information). Arrays of 50 × 50 nanodisks with different parameter combinations of s_d, L_c, and a random number generator seed values are fabricated on the same substrate. The disk diameter d is chosen as 120 nm, and the disk height h is 60 nm. A base lattice periodicity of P = 500 nm is used, so that diffraction modes of these arrays can be recorded using a sufficiently high microscope objective (NA). Additionally, arrays using the same disorder parameters but a periodicity of 250 nm are fabricated to obtain subdiffraction structures with a first-order diffraction that is not accessible through the microscope objective. The unperturbed arrays thus measure 25 × 25 and 12.5 × 12.5 μm^2 in size, respectively. SEM images of disordered nanodisk arrays can be found in the Supporting Information.

Measurement Setup. The microspectroscopy setup consists of a Nikon Eclipse TE2000-U inverted microscope in combination with a Princeton Instruments SP2500 grating spectrometer with a Pixis-256e Peltier-cooled CCD camera. The microscope and the spectrometer are connected *via* a modified 4-f setup,[56] in which a Bertrand lens is used to project the Fourier image onto the spectrometer entrance slit. For transmittance measurements, the sample is illuminated by a fiber-coupled halogen lamp using critical illumination under a maximum NA of 0.65, and the transmitted light is collected using a Nikon TU Plan Fluor ELWD 60× objective (NA 0.70). For reflectance measurements with near-zero NA illumination, the sample is illuminated by a fiber-coupled white light lamp (Energetiq EQ-99xfc) through a pinhole (50 μm) and a Köhler illumination path. To access a range of collection angles as large as possible, a high-resolution Nikon Plan Apo VC 100× oil-immersion objective with an NA of 1.40 is used. RGB image recording is performed using an Allied Vision Prosilica GC2450c CCD camera. In addition to RGB images of the nanodisk arrays, an image of the empty substrate is recorded to perform a background correction. This is necessary to eliminate the effects of substrate reflection and back reflections from the optical setup. Further details on the experimental setup and the background correction can be found in the Supporting Information.

ASSOCIATED CONTENT

Supporting Information

The Supporting Information is available free of charge at https://pubs.acs.org/doi/10.1021/acsnano.1c02538.

> SEM images of disordered nanoantennas arrays; detailed description of the measurement setup; color theory for conversion of spectral power distribution to visible color; background correction of recorded RGB images; calculation of the polarizability tensor; single-particle measurements and comparison to calculations (PDF)

AUTHOR INFORMATION

Corresponding Author

Harald Giessen − *4th Physics Institute and Research Center SCoPE, University of Stuttgart, 70569 Stuttgart, Germany*; Email: giessen@pi4.uni-stuttgart.de

Authors

Florian Sterl − *4th Physics Institute and Research Center SCoPE, University of Stuttgart, 70569 Stuttgart, Germany*; orcid.org/0000-0002-1025-6777
Ediz Herkert − *4th Physics Institute and Research Center SCoPE, University of Stuttgart, 70569 Stuttgart, Germany*
Steffen Both − *4th Physics Institute and Research Center SCoPE, University of Stuttgart, 70569 Stuttgart, Germany*
Thomas Weiss − *4th Physics Institute and Research Center SCoPE, University of Stuttgart, 70569 Stuttgart, Germany*; orcid.org/0000-0002-4991-6779

Complete contact information is available at: https://pubs.acs.org/10.1021/acsnano.1c02538

Author Contributions

The manuscript was written through contributions of all authors. All authors have given approval to the final version of the manuscript.

Notes

The authors declare no competing financial interest.

ACKNOWLEDGMENTS

We acknowledge financial support by the Deutsche Forschungsgemeinschaft (SPP1839 - Tailored Disorder), by the Bundesministerium für Bildung und Forschung, by the Baden-Württemberg Stiftung, by ERC Advanced Grant COMPLEXPLAS, and by the Ministerium für Wissenschaft, Forschung und Kunst Baden-Württemberg.

REFERENCES

(1) Moyroud, E.; Wenzel, T.; Middleton, R.; Rudall, P. J.; Banks, H.; Reed, A.; Mellers, G.; Killoran, P.; Westwood, M. M.; Steiner, U.; Vignolini, S.; Glover, B. J. Disorder in Convergent Floral Nanostructures Enhances Signalling to Bees. *Nature* **2017**, *550* (7677), 469−474.

(2) Meiers, D. T.; Heep, M. C.; Von Freymann, G. Invited Article: Bragg Stacks with Tailored Disorder Create Brilliant Whiteness. *APL Photonics* **2018**, *3* (10), 100802.

(3) Siddique, R. H.; Donie, Y. J.; Gomard, G.; Yalamanchili, S.; Merdzhanova, T.; Lemmer, U.; Hölscher, H. Bioinspired Phase-Separated Disordered Nanostructures for Thin Photovoltaic Absorbers. *Sci. Adv.* **2017**, *3* (10), e1700232.

(4) Cao, H. Lasing in Random Media. *Waves Random Media* **2003**, *13* (3), R1−R39.

(5) Vellekoop, I. M.; Lagendijk, A.; Mosk, A. P. Exploiting Disorder for Perfect Focusing. *Nat. Photonics* **2010**, *4* (5), 320−322.

(6) Huisman, S. R.; Huisman, T. J.; Goorden, S. A.; Mosk, A. P.; Pinkse, P. W. H. Programming Balanced Optical Beam Splitters in White Paint. *Opt. Express* **2014**, *22* (7), 8320.

(7) Huisman, S. R.; Huisman, T. J.; Wolterink, T. A. W.; Mosk, A. P.; Pinkse, P. W. H. Programmable Multiport Optical Circuits in Opaque Scattering Materials. *Opt. Express* **2015**, *23* (3), 3102.

(8) Jang, M.; Horie, Y.; Shibukawa, A.; Brake, J.; Liu, Y.; Kamali, S. M.; Arbabi, A.; Ruan, H.; Faraon, A.; Yang, C. Wavefront Shaping with Disorder-Engineered Metasurfaces. *Nat. Photonics* **2018**, *12* (2), 84−90.

(9) Koenderink, A. F.; Lagendijk, A.; Vos, W. L. Optical Extinction Due to Intrinsic Structural Variations of Photonic Crystals. *Phys. Rev. B: Condens. Matter Mater. Phys.* **2005**, *72* (15), 153102.

(10) Ren, L.; Chen, B. Proximity Effect in Electron Beam Lithography. *Int. Conf. Solid-State Integr. Circuits Technol. Proc., ICSICT* **2004**, *1*, 579−582.

(11) Kaspar, C.; Butschke, J.; Irmscher, M.; Martens, S.; Sailer, H.; Kirchner, R.; Guzenko, V. A.; Schift, H.; Burghartz, J. N. Adjustable Sidewall Slopes by Electron-Beam Exposure Layout. *J. Vac. Sci. Technol., B: Nanotechnol. Microelectron.: Mater., Process., Meas., Phenom.* **2017**, *35* (6), No. 06G501.

(12) Martins, E. R.; Li, J.; Liu, Y.; Depauw, V.; Chen, Z.; Zhou, J.; Krauss, T. F. Deterministic Quasi-Random Nanostructures for Photon Control. *Nat. Commun.* **2013**, *4*, 2665.

(13) Cherpakova, Z.; Bleckmann, F.; Vogler, T.; Linden, S. Transverse Anderson Localization of Surface Plasmon Polaritons. *Opt. Lett.* **2017**, *42* (11), 2165.

(14) Lalanne, P.; Yan, W.; Vynck, K.; Sauvan, C.; Hugonin, J. P. Light Interaction with Photonic and Plasmonic Resonances. *Laser Photonics Rev.* **2018**, *12* (5), 1−38.

(15) Redding, B.; Liew, S. F.; Sarma, R.; Cao, H. Compact Spectrometer Based on a Disordered Photonic Chip. *Nat. Photonics* **2013**, *7* (9), 746−751.

(16) Varytis, P.; Huynh, D.-N.; Hartmann, W.; Pernice, W.; Busch, K. Design Study of Random Spectrometers for Applications at Optical Frequencies. *Opt. Lett.* **2018**, *43* (13), 3180−3183.

(17) Maiwald, L.; Lang, S.; Jalas, D.; Renner, H.; Petrov, A. Y.; Eich, M. Ewald Sphere Construction for Structural Colors. *Opt. Express* **2018**, *26* (9), 11352.

(18) Rahimzadegan, A.; Arslan, D.; Suryadharma, R. N. S.; Fasold, S.; Falkner, M.; Pertsch, T.; Staude, I.; Rockstuhl, C. Disorder-Induced Phase Transitions in the Transmission of Dielectric Metasurfaces. *Phys. Rev. Lett.* **2019**, *122* (1), 15702.

(19) Neder, V.; Ra'Di, Y.; Alù, A.; Polman, A. Combined Metagratings for Efficient Broad-Angle Scattering Metasurface. *ACS Photonics* **2019**, *6* (4), 1010−1017.

(20) Mao, P.; Liu, C.; Song, F.; Han, M.; Maier, S. A.; Zhang, S. Manipulating Disordered Plasmonic Systems by External Cavity with Transition from Broadband Absorption to Reconfigurable Reflection. *Nat. Commun.* **2020**, *11* (1), 1538.

(21) Ferry, V. E.; Verschuuren, M. A.; Van Lare, M. C.; Schropp, R. E. I.; Atwater, H. A.; Polman, A. Optimized Spatial Correlations for Broadband Light Trapping Nanopatterns in High Efficiency Ultrathin Film A-Si:H Solar Cells. *Nano Lett.* **2011**, *11* (10), 4239−4245.

(22) Nanz, S.; Abass, A.; Piechulla, P. M.; Sprafke, A.; Wehrspohn, R. B.; Rockstuhl, C. Strategy for Tailoring the Size Distribution of Nanospheres to Optimize Rough Backreflectors of Solar Cells. *Opt. Express* **2018**, *26* (2), A111.

(23) Carlson, C.; Hughes, S. Disordered Nanophotonic Surfaces for Enhanced Light Collection in Semiconductor Solar Cells. *J. Opt. Soc. Am. B* **2018**, *35* (5), 1093−1104.

(24) Tavakoli, N.; Alarcon-Llado, E. Combining 1D and 2D Waveguiding in an Ultrathin GaAs NW/Si Tandem Solar Cell. *Opt. Express* **2019**, *27* (12), A909−A923.

(25) Tittl, A.; Harats, M. G.; Walter, R.; Yin, X.; Schäferling, M.; Liu, N.; Rapaport, R.; Giessen, H. Quantitative Angle-Resolved Small-Spot Reflectance Measurements on Plasmonic Perfect Absorbers: Impedance Matching and Disorder Effects. *ACS Nano* **2014**, *8* (10), 10885−10892.

(26) Sterl, F.; Strohfeldt, N.; Both, S.; Herkert, E.; Weiss, T.; Giessen, H. Design Principles for Sensitivity Optimization in Plasmonic Hydrogen Sensors. *ACS Sensors* **2020**, *5* (4), 917−927.

(27) Haghtalab, M.; Tamagnone, M.; Zhu, A. Y.; Safavi-Naeini, S.; Capasso, F. Ultrahigh Angular Selectivity of Disorder-Engineered Metasurfaces. *ACS Photonics* **2020**, *7* (4), 991−1000.

(28) Nicodemus, F. E. Reflectance Nomenclature and Directional Reflectance and Emissivity. *Appl. Opt.* **1970**, *9* (6), 1474.

(29) Dana, K. J.; Van Ginneken, B.; Nayar, S. K.; Koenderink, J. J. Reflectance and Texture of Real-World Surfaces. *ACM Trans. Graph.* **1999**, *18* (1), 1−34.

(30) Harms, J. D.; Bachmann, C. M.; Faulring, J. W.; Ruiz Torres, A. J. A Next Generation Field-Portable Goniometer System. *Proc. SPIE* **2016**, *9840*, 98400J.

(31) Dominguez, D.; Alharbi, N.; Alhusain, M.; Bernussi, A. A.; De Peralta, L. G. Fourier Plane Imaging Microscopy. *J. Appl. Phys.* **2014**, *116* (10), 103102.

(32) Bryche, J. F.; Barbillon, G.; Bartenlian, B.; Dujardin, G.; Boer-Duchemin, E.; Le Moal, E. K-Space Optical Microscopy of Nanoparticle Arrays: Opportunities and Artifacts. *J. Appl. Phys.* **2018**, *124* (4), No. 043102.

(33) Sersic, I.; Tuambilangana, C.; Koenderink, A. F. Fourier Microscopy of Single Plasmonic Scatterers. *New J. Phys.* **2011**, *13*, No. 083019.

(34) Röhrich, R.; Hoekmeijer, C.; Osorio, C. I.; Koenderink, A. F. Quantifying Single Plasmonic Nanostructure Far-Fields with Interferometric and Polarimetric k-Space Microscopy. *Light: Sci. Appl.* **2018**, *7* (1), 65.

(35) Shegai, T.; Chen, S.; Miljkovic, V. D.; Zengin, G.; Johansson, P.; Käll, M. A Bimetallic Nanoantenna for Directional Colour Routing. *Nat. Commun.* **2011**, *2* (1), 481.

(36) Vercruysse, D.; Sonnefraud, Y.; Verellen, N.; Fuchs, F. B.; Di Martino, G.; Lagae, L.; Moshchalkov, V. V.; Maier, S. A.; Van Dorpe, P. Unidirectional Side Scattering of Light by a Single-Element Nanoantenna. *Nano Lett.* **2013**, *13* (8), 3843−3849.

(37) Curto, A. G.; Taminiau, T. H.; Volpe, G.; Kreuzer, M. P.; Quidant, R.; Van Hulst, N. F. Multipolar Radiation of Quantum Emitters with Nanowire Optical Antennas. *Nat. Commun.* **2013**, *4*, 1750.

(38) Hancu, I. M.; Curto, A. G.; Castro-López, M.; Kuttge, M.; Van Hulst, N. F. Multipolar Interference for Directed Light Emission. *Nano Lett.* **2014**, *14* (1), 166−171.

(39) Lu, G.; Wang, Y.; Chou, R. Y.; Shen, H.; He, Y.; Cheng, Y.; Gong, Q. Directional Side Scattering of Light by a Single Plasmonic Trimer. *Laser Photonics Rev.* **2015**, *9* (5), 530−537.

(40) Neumaier, K. R.; Elender, G.; Sackmann, E.; Merkel, R. Ellipsometric Microscopy. *Europhys. Lett.* **2000**, *49* (1), 14−19.

(41) Linke, F.; Merkel, R. Quantitative Ellipsometric Microscopy at the Glass-Water Interface. *New J. Phys.* **2005**, *7* (1), 128.

(42) Harats, M. G.; Livneh, N.; Zaiats, G.; Yochelis, S.; Paltiel, Y.; Lifshitz, E.; Rapaport, R. Full Spectral and Angular Characterization of Highly Directional Emission from Nanocrystal Quantum Dots Positioned on Circular Plasmonic Lenses. *Nano Lett.* **2014**, *14* (10), 5766−5771.

(43) Fredriksson, H.; Alaverdyan, Y.; Dmitriev, A.; Langhammer, C.; Sutherland, D. S.; Zäch, M.; Kasemo, B. Hole-Mask Colloidal Lithography. *Adv. Mater.* **2007**, *19* (23), 4297−4302.

(44) Lau, C. Y.; Duan, H.; Wang, F.; He, C. Bin; Low, H. Y.; Yang, J. K. W. Enhanced Ordering in Gold Nanoparticles Self-Assembly through Excess Free Ligands. *Langmuir* **2011**, *27* (7), 3355−3360.

(45) Walter, R.; Tittl, A.; Berrier, A.; Sterl, F.; Weiss, T.; Giessen, H. Large-Area Low-Cost Tunable Plasmonic Perfect Absorber in the Near Infrared by Colloidal Etching Lithography. *Adv. Opt. Mater.* **2015**, *3* (3), 398−403.

(46) Herkert, E.; Sterl, F.; Strohfeldt, N.; Walter, R.; Giessen, H. Low Cost Hydrogen Sensor in the Ppm Range with Purely Optical Read-Out. *ACS Sensors* **2020**, *5* (4), 978−983.

(47) Piechulla, P. M.; Muehlenbein, L.; Wehrspohn, R. B.; Nanz, S.; Abass, A.; Rockstuhl, C.; Sprafke, A. Fabrication of Nearly-Hyperuniform Substrates by Tailored Disorder for Photonic Applications. *Adv. Opt. Mater.* **2018**, *6* (7), 1701272.

(48) Bauer, C.; Kobiela, G.; Giessen, H. 2D Quasiperiodic Plasmonic Crystals. *Sci. Rep.* **2012**, *2*, 1−6.

(49) Bauer, C.; Giessen, H. Optical Properties of Aperiodic Metallic Photonic Crystal Structures: Quasicrystals and Disorder. *J. Opt. (Bristol, U. K.)* **2014**, *16* (11), 114001.

(50) Torquato, S.; Stillinger, F. H. Local Density Fluctuations, Hyperuniformity, and Order Metrics. *Phys. Rev. E: Stat. Phys., Plasmas, Fluids, Relat. Interdiscip. Top.* **2003**, *68* (4), No. 041113.

(51) Nau, D.; Schönhardt, A.; Bauer, C.; Christ, A.; Zentgraf, T.; Kuhl, J.; Giessen, H. Disorder Issues in Metallic Photonic Crystals. *Phys. Status Solidi B* **2006**, *243* (10), 2331−2343.

(52) Nau, D.; Schönhardt, A.; Bauer, C.; Christ, A.; Zentgraf, T.; Kuhl, J.; Klein, M. W.; Giessen, H. Correlation Effects in Disordered Metallic Photonic Crystal Slabs. *Phys. Rev. Lett.* **2007**, *98* (13), 133902.

(53) Zhang, F.; Tang, F.; Xu, X.; Adam, P. M.; Martin, J.; Plain, J. Influence of Order-to-Disorder Transitions on the Optical Properties of the Aluminum Plasmonic Metasurface. *Nanoscale* **2020**, *12* (45), 23173−23182.

(54) Weiss, T.; Schäferling, M.; Giessen, H.; Gippius, N. A.; Tikhodeev, S. G.; Langbein, W.; Muljarov, E. A. Analytical Normalization of Resonant States in Photonic Crystal Slabs and Periodic Arrays of Nanoantennas at Oblique Incidence. *Phys. Rev. B: Condens. Matter Mater. Phys.* **2017**, *96* (4), No. 045129.

(55) Christ, A.; Zentgraf, T.; Kuhl, J.; Tikhodeev, S. G.; Gippius, N. A.; Giessen, H. Optical Properties of Planar Metallic Photonic Crystal Structures: Experiment and Theory. *Phys. Rev. B: Condens. Matter Mater. Phys.* **2004**, *70* (12), 125113.

(56) Kurvits, J. A.; Jiang, M.; Zia, R. Comparative Analysis of Imaging Configurations and Objectives for Fourier Microscopy. *J. Opt. Soc. Am. A* **2015**, *32* (11), 2082−2092.

(57) Fradkin, I. M.; Dyakov, S. A.; Gippius, N. A. Fourier Modal Method for the Description of Nanoparticle Lattices in the Dipole Approximation. *Phys. Rev. B: Condens. Matter Mater. Phys.* **2019**, *99* (7), No. 075310.

(58) Yang, J.; Hugonin, J. P.; Lalanne, P. Near-to-Far Field Transformations for Radiative and Guided Waves. *ACS Photonics* **2016**, *3* (3), 395−402.

(59) Knight, M. W.; King, N. S.; Liu, L.; Everitt, H. O.; Nordlander, P.; Halas, N. J. Aluminum for Plasmonics. *ACS Nano* **2014**, *8* (1), 834−840.

(60) Fasold, S.; Linß, S.; Kawde, T.; Falkner, M.; Decker, M.; Pertsch, T.; Staude, I. Disorder-Enabled Pure Chirality in Bilayer Plasmonic Metasurfaces. *ACS Photonics* **2018**, *5* (5), 1773−1778.

(61) Khorasaninejad, M.; Chen, W. T.; Devlin, R. C.; Oh, J.; Zhu, A. Y.; Capasso, F. Metalenses at Visible Wavelengths: Diffraction-Limited Focusing and Subwavelength Resolution Imaging. *Science* **2016**, *352* (6290), 1190−1194.

(62) Yin, X.; Steinle, T.; Huang, L.; Taubner, T.; Wuttig, M.; Zentgraf, T.; Giessen, H. Beam Switching and Bifocal Zoom Lensing Using Active Plasmonic Metasurfaces. *Light: Sci. Appl.* **2017**, *6* (7), e17016.